Lithos 322 (2018) 238–249

Contents lists available at ScienceDirect

Lithos

journal homepage: www.elsevier.com/locate/lithos

Magmatic Mn-rich garnets in volcanic settings: Age and longevity of the magmatic plumbing system of the Miocene Ramadas volcanism (NW Argentina)

Federico Lucci [a,*], Federico Rossetti [a], Raul Becchio [b], Thomas Theye [c], Axel Gerdes [d], Joachim Opitz [c], Walter Baez [b], Lorenzo Bardelli [b], Gianfilippo De Astis [e], José Viramonte [b], Guido Giordano [a]

[a] Dipartimento di Scienze, Università Roma Tre, Roma, Italy
[b] Instituto Geonorte, Facultad de Ciencias Naturales, Universidad Nacional de Salta and CONICET, Salta, Argentina
[c] Institut für Mineralogie und Kristallchemie, Universität Stuttgart, Stuttgart, Germany
[d] Institut für Geowissenschaften, Goethe-Universität, Frankfurt am Main, Germany
[e] Istituto Nazionale di Geofisica e Vulcanologia, Sezione di Roma 1, Rome, Italy

ARTICLE INFO

Article history:
Received 11 June 2018
Accepted 16 October 2018
Available online 19 October 2018

Keywords:
Magmatic garnet
Zircon
Timing of magmatic plumbing system
Ramadas volcanic centre
Plinian eruption

ABSTRACT

The Miocene "Corte Blanco Tuff" rhyolite deposit is the product of a large volume and high intensity Plinian eruption from the solitary and monogenetic Ramadas Volcanic Centre (Central Andes, Province of Salta, NW Argentina). The "Corte Blanco Tuff" consists of vitreous tube pumices with rare euhedral sub-millimetric Mn-garnet phenocrysts, typically hosting inclusions of U-phases as zircon and monazite. Here, we present new textural, major and trace elemental analyses of garnet, zircon and glass that, combined with in situ U-(Th)-Pb zircon and monazite dating, are used to reconstruct the thermobaric environment of formation, age and longevity of the magmatic plumbing system of the Ramadas magma. The results indicate to a crystallization path of a peraluminous rhyolitic melt at shallow crustal levels (≤6 km), as sequentially tracked by the initial nucleation of zircon (780 °C at 9.16 Ma) and garnet (above or at ca. 700 °C), to the final monazite growth (660–670 °C, at 8.70 Ma) in a water-saturated (H_2O = 3–5 wt%) environment, shortly before the eruption started. These data (1) define for the first time the primary magmatic origin of Mn-garnet in a rhyolitic volcanic setting; (2) provide new partition coefficients of rare earth elements (REE) between natural garnet, zircon and rhyolitic melts; and (3) permit reconstruction of the magmatic processes that resulted in the Ramadas eruption. On a wider scale, our results document the spatio-temporal (*P-T* conditions, timing and longevity) time scales involved in the petrogenesis of a shallow peraluminous water-saturated rhyolitic magmatic plumbing system that is able to generate the conditions for extremely explosive Plinian eruptions.

1. Introduction

Although garnet is a relatively common mineral phase in magmatic igneous rocks and it is mainly reported from very felsic peraluminous granitoids and from aplite and pegmatite granitoids (e.g., Gadas et al., 2013; Müller et al., 2012; Samadi et al., 2014), it is an uncommon accessory phase in volcanic rocks (e.g., Harangi et al., 2001 and references therein). In the last decade many studies have focused on the significance of garnet in felsic magmatic systems (e.g., Hönig et al., 2014; Lackey et al., 2012; Rubatto and Hermann, 2007; Samadi et al., 2014; Taylor et al., 2015; Taylor and Stevens, 2010; Zhou et al., 2017). Zhou et al. (2017) review the petrogenetic scenarios that result in the formation of garnet in magmatic systems: (i) restitic origin during a partial melting event; (ii) xenocrysts from metamorphic wall-rocks; (iii) peritectic genesis from wall-rock/xenolith materials reacting with magma; (iv) primary magmatic crystallization from ortho-magmatic to late-stage in fluid-rich aplite and pegmatite; and (v) secondary metasomatic origin by interaction between late- to post-magmatic fluids and the host SiO_2-rich felsic rock. The integration of petrography with major and trace elements is considered to be the key to understanding the origin of garnet from these settings (Taylor et al., 2015; Villaros et al., 2009a; Villaros et al., 2009b; Zhou et al., 2017). However, whereas there is a wide literature dealing with the origin of garnets from granitoids (e.g., Villaros et al., 2009a; Villaros et al., 2009b; Ma et al., 2017), skarn (e.g., Rossetti et al., 2007), metapelitic (e.g., White et al., 2014) and ultramafic (e.g., Evans and Trommsdorff, 1978; Zhang et al., 1994) rocks, there has been much less work on garnet from aplite-pegmatite melts (e.g., London, 2008; Villaros et al., 2009b, Villaros et al., 2009a; Taylor and Stevens, 2010; Müller et al., 2012; Gadas et al., 2013;

* Corresponding author.
E-mail address: federico.lucci@uniroma3.it (F. Lucci).

https://doi.org/10.1016/j.lithos.2018.10.016
0024-4937/

Samadi et al., 2014; Taylor et al., 2015) and in felsic volcanism (Clemens and Wall, 1984; Kawabata and Takafuji, 2005; Oliver, 1956; Patranabis-Deb et al., 2009; Wood, 1974; Wyborn et al., 1981). Mn-rich garnets in rhyolitic explosive products have only been reported in a few instances (e.g., Caffe et al., 2012; Mitropoulos et al., 1999; Viramonte et al., 1984).

Most of the existing work in relation to garnet in rhyolite assess its primary origin mainly on the basis of garnet composition (Caffe et al., 2012; Clemens and Wall, 1984; Mitropoulos et al., 1999; Oliver, 1956; Patranabis-Deb et al., 2009; Wood, 1974; Wyborn et al., 1981). However, garnet chemistry alone is not a conclusive criterion in determining its origin, as garnet in metamorphic rocks can have a wide compositional range depending on the bulk rock composition, local matrix composition around the garnet crystal, mineral assemblage and *P-T* conditions (e.g., Kawabata and Takafuji, 2005; Spear, 1993). Kawabata and Takafuji (2005) showed that magmatic garnets could be distinguished from metamorphic xenocrysts by the presence of minute glass/melt inclusions, indicating garnet growth in the presence of coexisting melt. However, this criterion is not able to discriminate between garnet of peritectic (metamorphic) and magmatic origin, since both are formed in the presence of melt and show similar characteristics such as melt inclusions (e.g., Cesare et al., 1997; Villaros et al., 2009a). No existing study has, therefore, clearly demonstrated the primary magmatic origin of Mn-rich garnets in volcanic rhyolitic setting.

The Miocene Corte Blanco Tuff (CBT), from the monogenetic Ramadas Volcanic Centre (RVC) in NW Argentina (Fig. 1a), is a Mn-garnet-bearing rhyolitic glassy pumice fall deposit, erupted by one of the largest Plinian eruptions in the Andes (Viramonte et al., 1994). This rhyolite is unique for the extremely high magma ascent rates (Marti et al., 1999) and for being sourced straight off the basement rocks of the Altiplano Puna plateau (Gauthier et al., 1994; Tait et al., 2009; Viramonte et al., 1994). Garnet is the only phenocryst present in the glassy matrix of the CBT and, consequently, the understanding of the spatio-temporal scales and physical-chemical processes involved in its genesis is essential to assess the evolution of the magmatic plumbing systems leading to the RVC Plinian volcanism.

In this study, we integrate textural observation and major and trace elemental analyses of mineral phases and glass with U-Th-Pb geochronology of the U-bearing phases (zircon and monazite) hosted as mineral inclusions in garnet phenocrysts, in order to understand the garnet origin and the temporal scales involved in magma genesis and explosive volcanism. The results permit to define (i) the magmatic origin of the Mn-rich garnets and (ii) the longevity of the Ramadas rhyolite melt from its genesis/crystallization history to its eruption.

2. Geological setting

The RVC is located in the province of Salta (NW Argentina), 10 km north of San Antonio de los Cobres town (Fig. 1a). The study area is part of the Altiplano Puna plateau and is situated north to the active trace of the NW-SE trending Calama-Olacapato-Toro (COT *auct.*) fault zone (Giordano et al., 2013; Viramonte et al., 1984). The RVC is a solitary and monogenetic centre, located at the footwall of a major N-S thrust that bounds the Sierra de San Antonio de los Cobres (Fig. 1a), where the low-grade Precambrian metamorphic basement rocks of the Puncoviscana Fm. are exposed (e.g., Tait et al., 2009).

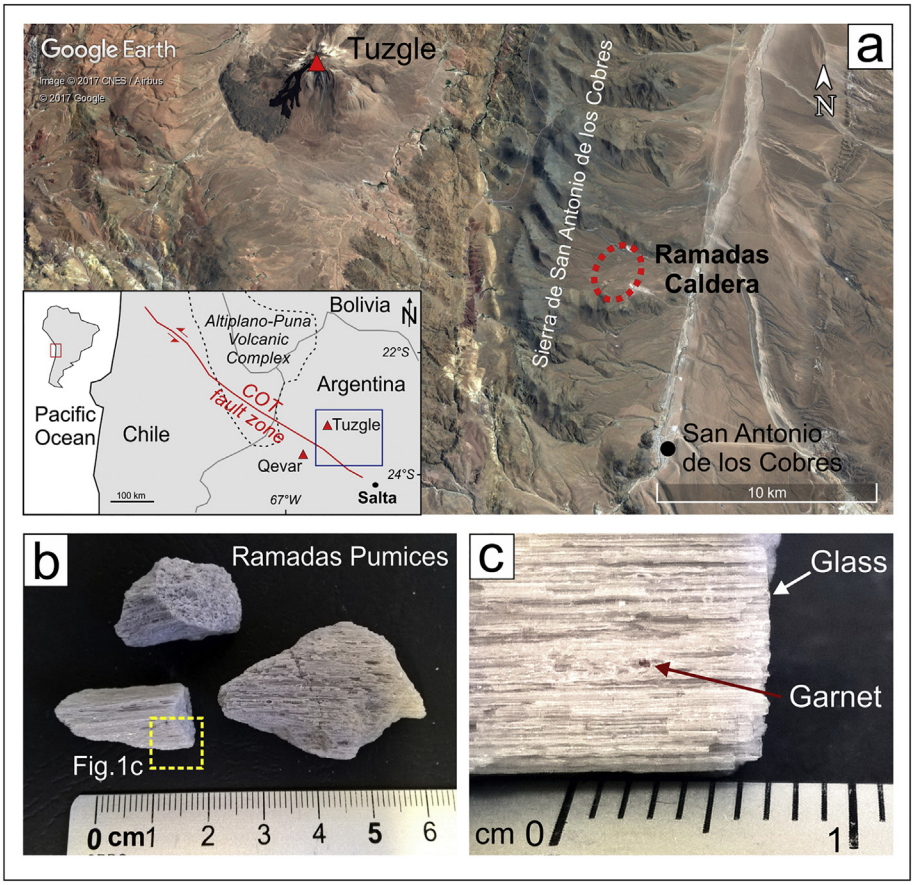

Fig. 1. Regional Context. (a) Satellite image of the Puna plateau area comprised between San Antonio de Los Cobres town and the Cerro Tuzgle volcano. The red dashed ellipse indicates the Ramadas Caldera. The inset box (bottom left) shows the the study area (blue rectangle) with respect to the major NW-SE left lateral Calama-Olocapato-Toro (COT) fault zone (modified after Giordano et al., 2013). (b) Hand samples of the garnet-bearing rhyolite Ramadas tube-pumice (meaning of Marti et al., 1999). (c) Enlargement of area indicated in (b) showing the tube-pumice glassy texture, characterized by stretched bubbles and vesicle tubes, and the rare, red-ruby garnet. (For interpretation of the references to colour in this figure legend, the reader is referred to the web version of this article.)

The RVC erupted only rhyolite, almost aphyric, with the presence of ca. 1% vol. of Mn-garnet (Gauthier et al., 1994; Viramonte et al., 1994). The eruption was Plinian and emplaced >30 km^3 of tube pumice fall deposit of the CBT, which are widely dispersed in north Argentina (Coira et al., 2018; Tait et al., 2009; Viramonte et al., 1994). The volume and the dispersal of the Corte Blanco fall deposit relate to an extremely explosive eruption from a flaring point vent structure (Dingwell et al., 2016; Tait et al., 2009). The tube pumices were studied in detail and allowed to define extremely high magma ascent rates and brittle failure of the melt at fragmentation, supporting the intensity of the eruption (Dingwell et al., 2016; Marti et al., 1999). During the late stage of the eruption, the degassed rhyolite magma emplaced small volume phreatomagmatic deposits and obsidian lavas within a ca. 12 km^2 wide depression, interpreted as a funnel caldera (Casas et al., 1995; Gauthier et al., 1994; Tait et al., 2009; Viramonte et al., 1994).

Different age determinations are available for the RVC deposits, spanning from 8.75 ± 0.25 Ma for the garnet-bearing rhyolite tube pumice (whole rock and glass K-Ar dating; Viramonte et al., 1994), 8.4 ± 0.3 Ma for the ignimbrite deposits (biotite K-Ar dating; Petrinovic et al., 1999), to 6.63 ± 0.28 Ma for the obsidian facies deposits (fission track ages; Tait et al., 2009), and 6.3 ± 0.28 Ma for the distal deposits (glass shard Ar-Ar dating; Coira et al., 2018).

3. Materials and methods

Garnet-bearing pumice samples from the CBT rhyolite were selected for petrographical investigation, mineral and whole-rock geochemistry (major and trace elements). Garnet crystals were separated by handpicking from ca. 5 kg of crushed, proximal (very fresh) rhyolitic pumices. Details on the following analytical procedures and techniques are given in the Appendix A. Mineral abbreviations follow Whitney and Evans (2010).

3.1. Whole-rock geochemistry

After washing in distilled water, samples were grounded in an agate mill, pre-contaminated with an aliquot of sample. The elemental analyses were performed at the Activation Laboratory (Ontario, Canada), through ICP emission (major and some trace elements) and ICP-MS for trace elements.

3.2. Mineral chemistry

Garnet and glass major element compositions were obtained using a Cameca SX100 electron microprobe at the Institut für Mineralogie, Universität Stuttgart. Trace and REE compositions of garnet and garnet-hosted inclusions of zircon were obtained through in situ sampling on polished mounts through a laser ablation inductively coupled plasma mass spectrometry (LA-ICP-MS) at the Institut für Mineralogie, Universität Stuttgart.

3.3. U–Pb zircon and monazite geochronology

Garnet-hosted inclusions of zircon and monazite grains were first investigated through cathodoluminescence (CL) and back-scattered electron (BSE) imaging techniques and then analyzed in situ through a LA-ICP-MS system at the Goethe University of Frankfurt.

4. Petrography

The CBT rhyolite is made of homogeneous white glassy rhyolitic, lapilli-sized, tube pumices (Fig. 1b), with rare ruby-red garnets (< 1% vol., average grain size <0.3 mm; Figs. 1c and 2a) (Gauthier et al., 1994; Marti et al., 1999; Viramonte et al., 1994). In thin section, pumices show a fabric dominated by highly stretched bubbles (Fig. 2b). Garnets show euhedral habit, defined by trapezohedron and dodecahedron morphology (Fig. 2c). These textural characteristics suggest original equilibrium texture between garnet and glass. Garnet typically hosts inclusions of zircon with euhedral prismatic (elongated-to-short) bipyramidal habit and rare monazite crystals (Figs. 2a, d).

5. Mineral chemistry

5.1. Garnet

Representative major element compositions and formulae for the CBT garnets are reported in Table 1 (see Supplementary Table S1 for the complete dataset). Garnet is characterized by high FeO_{tot} (29.6–32.1 wt%) and MnO (9.47–10.69 wt%), and low CaO (1.11–1.38 wt%) and MgO (always <0.20 wt%). The ferric iron content (Fe^{3+} up to 0.142 apfu), as calculated on the basis of stoichiometric constraints, is mostly close to Ca (Ca up to 0.124 apfu), indicating that Ca is essentially present as the andradite component. The Y_2O_3 content varies between 0.3 and 0.6 wt%. Interestingly, there is always a small but reproducible Na content that is in the range of that of Y. It can be speculated that the substitution of Ca by Y is, at least partly, accommodated by an equal amount of Na according to 2Ca = Y + Na (Enami et al., 1995). The TiO_2, ZrO_2, Cr_2O_3, and Ce_2O_3 contents are always below the detection limit of the microprobe (see Appendix A1). Consequently, the CBT garnet predominantly corresponds to an almandine-spessartine solid solution with pyrope + andradite + YAG always minor than 5% ($Alm_{69\text{-}71}Sps_{23\text{–}25}Andr_4Prp_1$).

The core-to-rim chemical zonation was investigated in two selected, inclusion free, specimens (Figs. 3a-b). The chemical zonation is mainly characterized by an oscillatory and rimward decrease of the Y_2O_3 content (core 0.47–0.58 wt%; rim 0.28 wt%), locally associated with a sensitive variation of the CaO content (1.20–1.38 wt%) (Figs. 3c-f).

Representative trace and REE elements data for the Ramadas garnets are presented in Table 2 (see Supplementary Table S2 for the complete dataset). All garnets show low light rare earth (LREE, with ΣLREEs always <25 ppm) and high heavy rare earth (HREE, with ΣHREEs ranging 1700–2610 ppm) elements contents, respectively. When normalized to Chondrite (Sun and McDonough, 1989), garnets show depleted LREE profiles (with La_N/Sm_N and La_N/Yb_N mean values of 0.06 and 0.001, respectively), opposed to enriched, bell-shaped HREEs profiles (Dy_N/Yb_N values of 0.60–0.76) (Fig. 4). All garnets show negative Eu anomaly (defined as $Eu^* = Eu_N/[(Sm_N \times Gd_N)^{1/2}]$), ranging 0.010–0.015. A general rimward decrease of the high field strength elements (HFSE) is documented (from core to rim: Ti 79–43 ppm; Zr 113–14 ppm; Nb 0.91–0.02 ppm; Y 5407–2950 ppm; Dy 729–434 ppm; and Yb 678–416 ppm).

5.2. Zircon

Five zircons were analyzed in situ for trace and REEs elements. Representative results from LA-ICP-MS analyses are presented in Table 2 (see Supplementary Table S2 for the complete dataset). They present high contents of HFSE as Dy, Yb, Y, Hf, Ta, Th and U together with enrichment of Nb (19.8–49.6 ppm) and Ti (6.7–28.8 ppm). All analyzed crystals are characterized by low LREE (ΣLREEs ranging 22–168 ppm) and high HREE (ΣHREEs ranging 2545–9830 ppm,) contents, respectively. In Chondrite-normalized (Sun and McDonough, 1989) diagrams, zircons show depleted LREE profiles (La_N/Sm_N values ranging 0.01–0.10) opposite to highly enriched HREE profiles (Dy_N/Yb_N values ranging 0.21–0.45) (Fig. 4). Systematically, all the analyzed zircons are depleted in Eu ($Eu^* = 0.01–0.04$).

Based on the crystal morphology and texture (Figs. 2a, d) and the REE/chondrite profiles (Fig. 4), the hosted zircons are comparable to those reported from water-bearing granitoid melts (Belousova et al., 2002; Hoskin and Schaltegger, 2003).

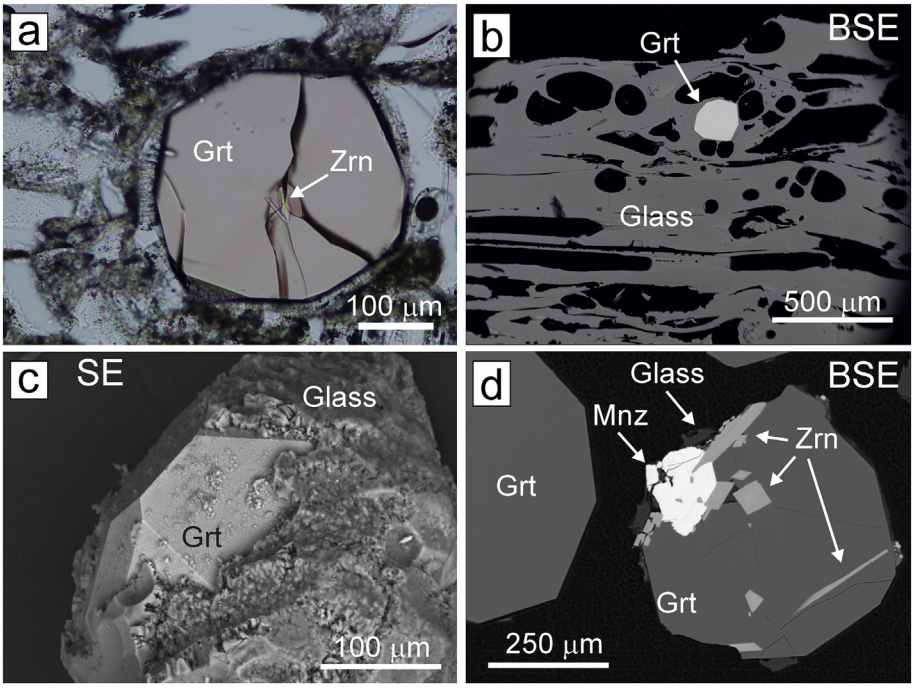

Fig. 2. Microtexture of the Ramadas tube-pumices. (a) Euhedral garnet (Grt) in the glass matrix, hosting prismatic zircons (Zrn) (normal polars). (b) Back-scattered electrons (BSE) image of the pumice fabric, dominated by stretched bubbles and vesicle tubes. The only visible mineral phase is represented by garnet. (c) Secondary electrons (SE) image of a separated single crystal of garnet showing the euhedral habit defined by trapezohedron in combination with dodecahedron morphology. (d) BSE image of garnet hosting inclusions of zircon and rare monazite (Mnz) crystals.

5.3. Volcanic glass

Results from EMPA analyses of glass are presented in Table 3. Volcanic glass is characterized by high SiO_2 content (72.2–74.6 wt%), low CaO (0.52–0.62 wt%), FeO_{tot} (0.74–0.88 wt%), MgO (<0.02 wt%) and MnO (0.07–0.18 wt%). All glass-spots show enrichment in K_2O (4.03–5.56 wt%) with respect to Na_2O (0.96–1.46 wt%) and Al_2O_3 in the range 12.89–13.49 wt%. The contents of MgO, TiO_2, ZrO_2, and Y_2O_3 are always below the detection limit of the microprobe. The difference from 100% of the total oxides, attributed to H_2O content, has a mean value of 5.17 wt%. BSE images and chemical analyses showed that there is neither significant zoning in the glass nor chemical variations in the glass surrounding garnets. These compositions attest for a high-K calc-alkaline rhyolite composition with a strong peraluminous signature, with ASI (Alumina Saturation Index, molar $[Al_2O_3/(CaO + Na_2O + K_2O)]$) values of 1.47–1.82.

A whole-pumice, its separated glass and its enriched Grt (+ zircon + monazite) fraction were analyzed for major, trace and REE elements. Results from ICP-MS are reported in Table 4. The whole-pumice and the separated glass show the same REE pattern (Fig. 4). Whole-pumice and glass are slightly enriched in LREE (ΣLREE: 39.8–41 ppm) and in HREE (ΣHREE: 11.6–12.9 ppm). When normalized to Chondrite (Sun and McDonough, 1989) they have a flat profile, with a pronounced negative Eu anomaly (ca. 0.06) (Fig. 4). When compared with the Grt (+ zircon + monazite) fraction, they are depleted in HFSE and actinides, as indicated by low contents of Y (21.8–24 vs. 3080 ppm), Zr (31–34 vs. 1391 ppm), Yb (0.9–1.21 vs. 439 ppm), Th (7.61–7.83 vs. 119 ppm) and U (10.6 vs. 49.3 ppm) (Table 4). When normalized to Chondrite (Sun and McDonough, 1989), the Grt (+ zircon + monazite) fraction shows a strongly enriched pattern (Fig. 4).

Table 1
Representative Electron Microprobe analyses and chemical formulae of garnets.

Sample[a]	Garnet core		Garnet rim	
Specimen	Grt1	Grt9	Grt11	Grt9
Spot	#10	#18	#34	#26
SiO_2, wt%	34.8	35.3	35.2	35.3
Al_2O_3	19.72	19.98	20.00	20.02
FeO_{tot}	31.7	31.1	30.7	31.6
MnO	10.29	10.42	9.87	10.15
MgO	0.16	0.13	0.16	0.18
CaO	1.33	1.24	1.19	1.17
Na_2O	0.07	0.05	0.04	0.03
Y_2O_3	0.58	0.47	0.31	0.35
Total	98.71	98.64	97.49	98.83
Si, apfu	2.921	2.955	2.981	2.953
Al	1.949	1.972	1.994	1.972
Fe^{3+}	0.130	0.073	0.025	0.076
Fe^{2+}	2.093	2.104	2.145	2.134
Mn	0.731	0.740	0.707	0.718
Mg	0.020	0.016	0.020	0.022
Na	0.011	0.008	0.007	0.006
Ca	0.120	0.112	0.108	0.105
Y	0.026	0.021	0.014	0.015
Gross/Andr (X_{mol})	0.04	0.04	0.04	0.03
Spessartine	0.24	0.25	0.24	0.24
Pyrope	0.01	0.01	0.01	0.01
Almandine	0.70	0.70	0.71	0.71

The contents of P_2O_5, TiO_2, ZrO_2, and Ce_2O_3 are below detection limits of 0.05, 0.03, 0.14, and 0.13 wt%, respectively.
[a] FeO_{tot} total iron reported as FeO; apfu: atoms per formula unit.

6. Zircon and monazite U-(Th)-Pb geochronology

The zircon and monazite inclusion hosted in garnet were analyzed for U, Th and Pb isotopic compositions using a LA-ICP-MS system (see the Appendix for the analytical protocols). Plots and age calculations were made using the ISOPLOT software (Ludwig, 2010). Results are shown Fig. 5 and listed in Supplementary Table S3.

The BSE and CL images reveal a homogeneous zircon population (grain size: 50–200 μm) characterized by oscillatory zoning (Fig. 5), a texture that is typical of magmatic crystallization (e.g., Corfu et al.,

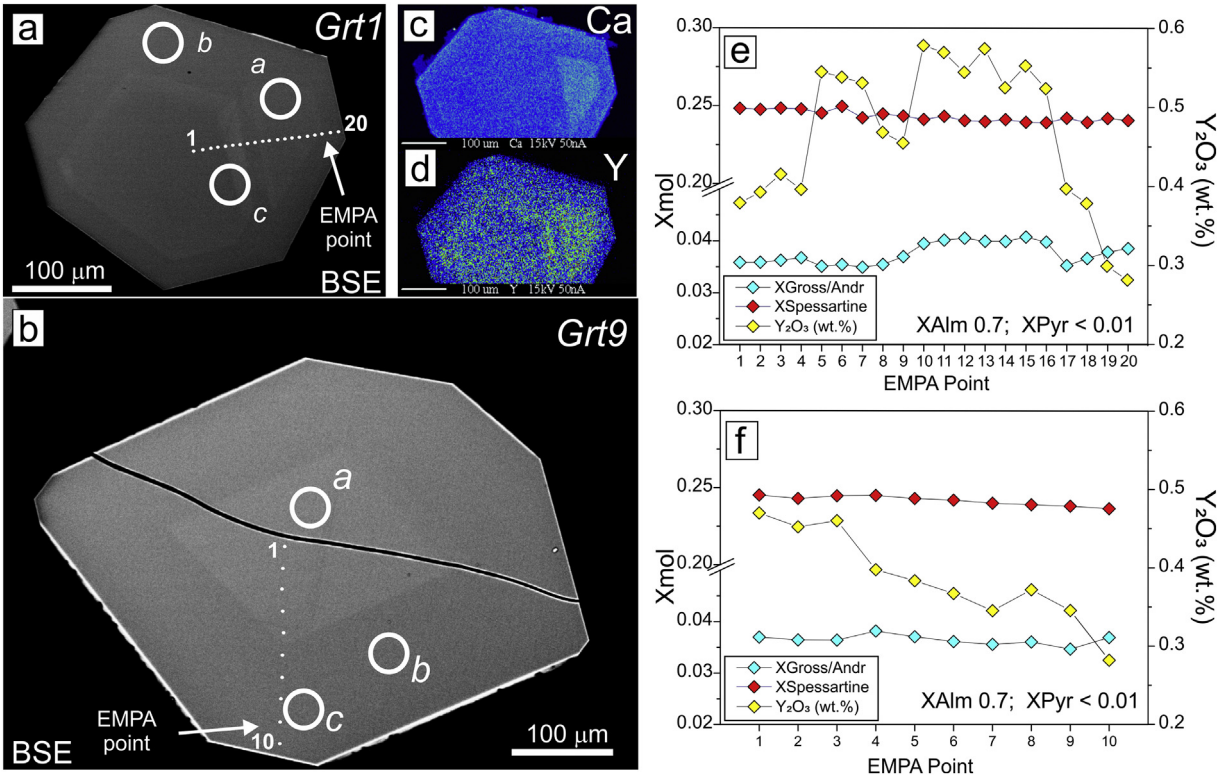

Fig. 3. Garnet chemistry. (a-b) BSE images of garnet displaying faint oscillatory zoned cores. The circles indicate the laser ablation spots used for in situ LA-ICP-MS trace and REE chemistry. The white points (numbered as 1 to 20 and 1 to 10, respectively) indicate the EMPA compositional line traverses shown in (e) and (f), respectively. (c-d) Qualitative compositional map showing variation in cation (Ca, Y) distribution of the garnet crystal shown in (a). (e) EMPA composition profile of the garnet shown in (a). (f) EMPA composition profile of the garnet shown in (b).

2003; Harley et al., 2007). Monazite is relatively coarse-grained (commonly 50–150 μm), with subhedral habit; Figs. 2d, 5a-b, 5e-h. Thirty spots (20–30 μm in diameter) on twenty-one zircons yielded a unimodal age distribution with a Concordia age of 9.16 ± 0.04 Ma (Fig. 5i). Twenty spots (30 μm in diameter) on fourteen monazite grains provided a well-defined Concordia age of 8.70 ± 0.23 Ma (Fig. 5l).

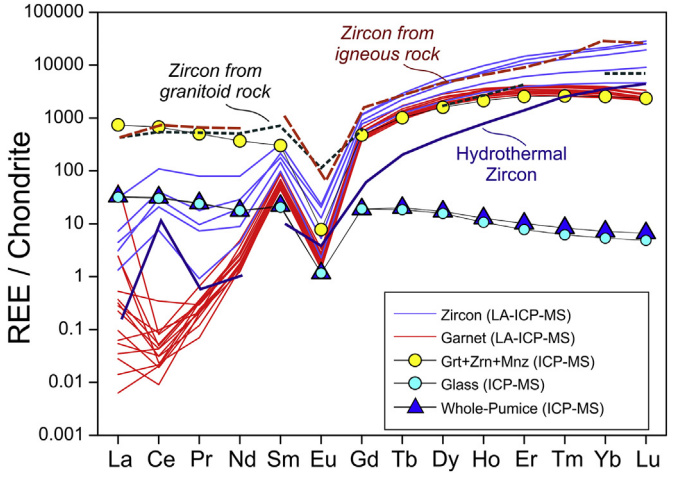

Fig. 4. Chondrite-normalized (after Sun and McDonough, 1989) rare earth elements (REE) spider diagram for the Ramadas rhyolite tube-pumice. Chondrite-normalized averaged REE patterns from literature are also reported: zircon from granitoid rocks (Belousova et al., 2002); zircon from igneous rocks (Hoskin and Schaltegger, 2003); and zircon crystallized under conditions of high aqueous-fluid activity at the end of the magmatic crystallization (hydrothermal zircon) from Mole Granite (SW Australia) (Hoskin and Schaltegger, 2003).

7. Thermobarometry

To assess the pressure-temperature (*P-T*) environment of formation of the Ramadas rhyolitic magma, we integrate inverse thermobarometry, as derived from the Ti-in-Zircon thermometry (Ferry and Watson, 2007; Watson et al., 2006), Zircon-saturation thermometry (T_{Zr}, Watson and Harrison, 1983), and the Monazite-solubility model (T_{REE}, Montel, 1993).

7.1. Ti-in-Zircon thermometry

Ti-in-Zircon thermometry has wide application to igneous and metamorphic rocks and ore deposits. The thermometer can be applied to individual zircon grains, providing independently estimates of temperature of their crystallization. Zircon inclusions in Ramadas garnets invariably show (i) the absence of inherited cores, (ii) prismatic habit, and (iii) oscillatory zoning typical of magmatic crystallization. Therefore, the Ti-in-Zircon thermometry likely indicates the temperature at which zircons crystallized from the melt.

The Ti content in zircon inclusions hosted in garnet ranges 6.76–28.81 ppm and application of the Ti-in-Zircon thermometry of Ferry and Watson (2007) for rutile- and quartz-free rocks indicates temperatures in the range 710–856 °C (in Table 2), with a mean value of ≈ 785 ± 70 °C (n = 5). Results variability is compatible with maximum uncertainties of ca. 60–70 °C at 750 °C for rutile- and quartz-free rocks as assessed by Ferry and Watson (2007).

7.2. Zircon-saturation thermometry and Monazite-solubility model

The zircon-saturation model was built to provide information on saturation behavior of zircon in hydrous, metaluminous to peraluminous, intermediate to felsic magma types (Watson and Harrison, 1983). Moreover, the zircon-saturation model provides good

Table 2
Representative selected trace and REE elements as obtained through in situ LA-ICP-MS analyses of garnets and hosted zircon inclusions.

Sample	Garnet-9			Zircon Inclusions		
Specimen	Grt9	Grt9	Grt9	Zrn2	Zrn3	Zrn7
Spot	RAGT9a	RAGT9b	RAGT9c	Zr2a	Zr3a	Zr7a
Trace elements (ppm)						
Sc	120.27	91.37	93.97			
Ti	44.98	43.78	52.35	6.76	12.41	28.81
Cr	4.39	3.49	3.15	10.85	4.86	4.21
Ni	2.12	1.88	1.76			
Ga	31.28	26.51	26.89	4.75	8.28	18.17
Y	3777.27	3052.60	2952.02	9304.41	17,371.38	12,060.40
Zr	20.16	15.01	14.87			
Nb	0.89	0.06	0.03	49.61	36.55	36.96
Ta	0.40	0.06	0.07	13.15	10.82	9.70
La	13.04	0.58	0.07	1.05	0.73	7.28
Ce	0.05	0.01	0.02	12.71	18.23	66.81
Pr	0.03	0.01	0.01	0.69	0.91	7.58
Nd	0.96	0.65	0.72	4.13	9.14	37.24
Sm	10.41	7.00	6.76	22.15	33.15	49.06
Eu	0.12	0.08	0.09	0.30	1.19	1.34
Gd	106.44	80.92	76.90	159.59	242.41	236.02
Tb	49.25	39.08	35.14	63.20	110.64	101.25
Dy	554.02	472.68	434.13	754.11	1505.26	1239.09
Ho	189.02	151.31	146.33	258.66	561.70	411.33
Er	682.68	533.89	494.07	1022.63	2478.68	1780.85
Tm	98.56	81.29	72.67	187.13	475.19	335.08
Yb	596.26	506.31	451.87	1377.22	3717.08	2700.28
Lu	74.72	61.19	56.64	234.35	737.89	501.19
Hf	1.19	0.74	0.79	17,442.85	16,151.94	12,702.62
Pb	0.29	0.04	0.04	4.76	2.22	5.21
Th	0.02	0.00	*bdl*	872.67	1165.24	784.39
U	0.11	0.03	0.04	7325.11	9998.63	6471.92
[(a)] T °C [± 70 °C]				710	767	856

bdl: below detection limit.
(a) Ti-in-Zircon thermometry (Ferry and Watson, 2007).

estimates of melt temperatures for crystal-poor magmatic rocks derived from zircon-saturated magmas (Miller et al., 2003). Since the Ramadas Grt-bearing rhyolite is crystal-poor and zircon-saturated, the temperature estimates likely indicate the temperature of the melt (glass) crystallization. Whole-pumices and glass show values of Zr in the range 31–34 ppm, corresponding to T_{Zr} of 666–672 ± 25 °C (Table 4).

Monazite-solubility model (Montel, 1993) describes the solubility of monazite in Ca-poor felsic/acid melt based on the REE content of a melt in equilibrium with monazite that is temperature dependent (REE-thermometry). The temperature indicated by this model is the temperature at which the monazite formed/equilibrated with the melt (Montel, 1993) and, in the case of obsidian/pumices glass, it is the temperature before the eruption (Rapp and Watson, 1986; Montel, 1993). This thermometer, as defined by Montel (1993), operates properly if (i) monazite controls the behavior of LREE in melt, and (ii) the whole-rock composition represents a frozen liquid.

Whereas garnet and zircon act as competitors for HREE, monazite is the unique phase controlling light REE (LREE). The REE enriched pattern of the garnet fraction confirms the control operated by the U-phases on the LREE (monazite) and HREE (zircon) budget (Fig. 4). Furthermore, considering that glass makes up ca. 99% of the rhyolite volume, it is possible to consider both whole-pumice and glass compositions as the liquid composition prior to eruption (Montel, 1993). Monazite-solubility model thus represents both the monazite-forming temperature and the temperature prior to the Ramadas eruption.

The solubility REE-temperatures were calculated for a H_2O content varying from 1 to 5 wt%. The zircon-saturation and the monazite-solubility models show convergence ($T_{REE} = T_{Zr} \pm 25$ °C) at $T = 660$–670 °C for a H_2O content in the range 3–5 wt% (Table 4). These calculated water contents are comparable to the EMPA estimates and are in agreement with those obtained by Dingwell et al. (2016) through micro-FTIR investigations on the RVC tube pumices. Following the experimental determination of water-solubility in silicate melts (Wallace and Anderson, 2000), the estimated water contents qualitatively indicates a lithostatic pressure of 1–1.5 kb for the RVC rhyolites. Assuming a rock density of 2600 kg/m^3, this pressure corresponds to depths <6 km for the formation of the Ramadas rhyolite melt.

8. Discussion

The Ramadas CBT rhyolite shows a high-K calc-alkaline peraluminous rhyolite composition. The main feature of this rhyolite is the presence of sub-millimetric Mn-garnet phenocrysts. In this study, we have documented their homogeneous core-to-rim major elements composition and the presence of zircon and monazite inclusions. The occurrence of U-bearing accessory phases in garnet with different radiometric closure temperatures (800 ± 50 °C for the U—Pb system in zircon and 700 ± 50 °C for the U-(Th)-Pb system in monazite; Carlson, 2011) allow to constrain the timing, rates and thermobaric environment of formation of the Ramadas garnet. Moreover, garnet and zircon act as competitors for partitioning HFSE and HREE elements (e.g., Rubatto, 2002; Rubatto and Hermann, 2003, 2007; Taylor et al., 2015; Taylor et al., 2017; Villaros et al., 2009a; Villaros et al., 2009b). Therefore, the assessment of the REE budget and their phase/melt and phase/phase distribution coefficients may provide a clue for (i) the understanding of the magmatic equilibria in the garnet-zircon-silicic melt system (Bea et al., 1994; Belousova et al., 2002; Hoskin and Schaltegger, 2003; Rubatto, 2002; Rubatto and Hermann, 2003, 2007; Taylor et al., 2015; Taylor et al., 2017; Villaros et al., 2009b; Watson and Harrison, 1983), and (ii) the origin of garnet in silicic melts and the longevity of the magmatic plumbing system.

Table 3
Representative analyses (EMPA) of volcanic glass from Ramadas tube-pumice.

Sample	RA (Ramadas Pumice Thin Section)											
Spot	#1	#2	#3	#4	#5	#6	#7	#8	#9	#10	#11	#12
SiO_2, wt%	74.0	74.0	74.6	74.4	74.1	74.4	74.3	74.3	74.5	74.2	72.9	72.3
Al_2O_3	13.45	13.37	13.28	13.37	13.18	13.36	13.35	13.22	13.27	13.36	13.31	12.89
FeO_{tot}	0.80	0.79	0.81	0.76	0.88	0.82	0.82	0.88	0.79	0.79	0.86	0.74
MnO	0.10	0.10	0.11	0.08	0.12	0.11	0.14	0.12	0.12	0.07	0.18	0.11
CaO	0.55	0.58	0.60	0.57	0.56	0.59	0.55	0.52	0.54	0.56	0.53	0.62
Na_2O	1.11	1.09	1.04	1.27	1.44	1.22	1.10	1.08	1.36	1.46	1.18	0.96
K_2O	4.22	4.38	5.36	5.04	4.61	5.57	5.40	5.40	4.97	4.04	4.62	4.30
Total	94.24	94.27	95.83	95.47	94.93	96.01	95.64	95.55	95.51	94.51	93.57	91.91
[(a)] ASI	1.82	1.76	1.54	1.56	1.57	1.47	1.54	1.54	1.54	1.71	1.68	1.75

(a) ASI = Alumina Saturation Index; molar [$Al_2O_3/(CaO + Na_2O + K_2O)$].
The contents of TiO_2, MgO, BaO, ZrO_2, and Y_2O_3 are below detection limits of 0.03, 0.03, 0.04, 0.06, and 0.07 wt%, respectively.

Table 4
ICP-MS compositional data of whole-pumice, glass and garnet separates.

Sample	Whole-Pumice	Glass	Grt + Zrn + Mnz
SiO_2, wt%	69.33	70.00	36.26
Al_2O_3	12.97	13.46	19.51
Fe_2O_{3tot}	1.53	1.37	33.47
MnO	0.11	0.10	8.66
MgO	0.22	0.21	0.24
CaO	0.63	0.69	1.24
Na_2O	3.04	2.97	0.22
K_2O	5.22	5.51	0.25
TiO_2	0.01	0.00	0.04
P_2O_5	0.03	0.03	0.07
LOI	5.93	6.55	*NA*
Total (wt%)	99.01	100.90	99.97
ASI	1.10	1.14	–
Sc, ppm	5	5	87
Be	9	10	< 1
V	< 5	< 5	14
Cr	< 20	< 20	20
Co	< 1	< 1	3
Ni	< 20	< 20	< 20
Cu	< 10	< 10	10
Zn	70	70	120
Ga	20	20	28
Ge	2.3	2.2	15.3
As	6	7	< 5
Rb	302	304	13
Sr	12	14	6
Y	24	21.8	3080
Zr	34	31	1391
Nb	15.7	17	2.2
Mo	< 2	< 2	7
Ag	< 0.5	< 0.5	4.5
In	< 0.1	< 0.1	< 0.1
Sn	7	7	3
Sb	< 0.2	0.2	0.2
Cs	27.6	28.1	1.7
Ba	6	5	11
La	7.8	7.52	177
Ce	19.3	18.6	416
Pr	2.34	2.27	48.1
Nd	8.26	8.29	173
Sm	3.35	3.13	46.4
Eu	0.067	0.067	0.449
Gd	3.88	3.91	98.9
Tb	0.75	0.69	38.3
Dy	4.33	3.97	410
Ho	0.72	0.6	122
Er	1.67	1.28	428
Tm	0.212	0.157	67.1
Yb	1.21	0.9	439
Lu	0.168	0.123	60.2
Hf	1.7	1.7	55.3
Ta	3.36	3.46	< 0.01
W	3.7	2.5	1.8
Tl	1.42	1.7	0.11
Pb	31	30	< 5
Bi	1	1.1	0.1
Th	7.83	7.61	119
U	10.6	10.6	49.3
La_N/Sm_N	1.503	1.551	2.462
La_N/Yb_N	4.623	5.993	0.289
Dy_N/Yb_N	2.395	2.952	0.625
Eu^*	0.057	0.059	0.02
[(a)] T_{Zr}(°C)	672	666	
[(b)] T_{REE}(°C) for H_2O = 3 wt%	677	678	
[(b)] T_{REE}(°C) for H_2O = 5 wt%	664	665	

Grt: Garnet; Zrn: Zircon; Mnz: Monazite.
Note: LOI: loss on ignition; NA: Not Available; ASI: molar $Al_2O_3/(CaO + Na_2O + K_2O)$; Eu^*: $Eu_N/[(Sm_N \times Gd_N)^{1/2}]$.
(a) T_{Zr} (°C) = Zircon saturation thermometry (Watson and Harrison, 1983)
(b) T_{REE}(°C) = LREE thermometry (Montel, 1993) calculated for different H_2O wt% content.

8.1. On garnet genesis and growth

Ramadas garnets are almandine-spessartine solid solutions ($Alm_{69-71}Sps_{23-25}$; Figs. 3 e-f), with a MnO content in the range 9.47–10.69 wt %, low CaO (< 1.4 wt%) and negligible MgO (< 0.2 wt%) contents. In a CaO vs. MnO proxy diagram (after Harangi et al., 2001) modified for Mn-garnet bearing aplites and pegmatites (Samadi et al., 2014), the Ramadas garnets fall at the intersection of "Metapelitic garnets" and "Aplite-Pegmatite garnets" fields (after Samadi et al., 2014 and references therein) (Fig. 6). When compared with the Mn-rich garnet compositions from the Neogene Coyaguayma ignimbrite (northern Puna, Argentina; Caffe et al., 2012) and the Chios rhyolite (Cyclades, Greece, Neogene in age; Mitropoulos et al., 1999), these garnet compositions show common features such as (i) the lack of Mn-zoning; (ii) a Mg# (Mg#: MgO/(MgO + FeO)) < 5; and (iii) a direct proportionality between Mn and Ca contents. Moreover, all the three reported volcanic garnet compositions fall outside the conventional fields for intrusive magmatic garnets (Fig. 6).

As shown by Yardley (1977) and Spear (1993), diffusion in garnet becomes exponentially more rapid with increasing temperature, and diffusion rates for Mn in garnet are negligible below ca. 650 ± 30 °C (Harrison, 1988; Manning, 1983; Yardley, 1977). By contrast, self-diffusion of Mn in spessartine-almandine garnet above ca. 700 °C is sufficiently rapid to re-equilibrate any compositional zoning during crystal growth (Dahlquist et al., 2007). Unzoned profiles are, then, expected for magmatic garnets crystallizing above ca. 700 °C (e.g., Dahlquist et al., 2007; Harrison, 1988; Manning, 1983; Miller and Stoddard, 1981; Spear, 1993; Yardley, 1977). The Ramadas garnets are unzoned ($Alm_{69-71}Sps_{23-25}$; Figs. 3e-f) and the absence of a rimward Mn enrichment indicates the garnet crystallization ceased above or near ca. 700 °C.

The Ramadas garnets show a positive correlation between Y and ΣREE contents, with the maximum values at cores. Similar patterns of rimward depletion are also recognized for the HFSE (such as Zr, Nb, Ti) which could be related to melt genesis processes (Smeds, 1994), or fluid-phase accumulation in melt that hindered the entrance of REE in the garnet structure (Wang et al., 2003). These observations are not sufficient to discriminate between garnets formed during progressive anatexis at depth (peritectic garnet) and primary magmatic garnets formed during crystallization, since both form in the presence of melt (Cesare et al., 1997; Villaros et al., 2009b). However, evidence of the primary magmatic origin for the Ramadas garnets is provided by: (i) the euhedral crystal shape, with no indication of resorption processes, (ii) the flat Mn zonation patterns and the lack of Fe-Mg-Mn zoning that is typical of high crystallization temperature (>700 °C), (iii) absence of metamorphic mineral inclusion, (iv) inclusions of magmatic accessory phases such as zircon and monazite, and (v) the strong negative Eu anomaly (< 0.02) of the garnet grains (Fig. 4), consistent with garnet growth from a high-SiO_2 melt (Dahlquist et al., 2007; Samadi et al., 2014; Taylor et al., 2015; Villaros et al., 2009b; and references therein). Moreover, the pressure estimates of 1–1.5 kbar obtained in this work by application of the water-solubility model (Wallace and Anderson, 2000) is in good agreement with the pressure of 1 kbar indicated by Clemens and Wall (1981, 1988) for the Mn-rich almandine garnet formation in S-type felsic melts (cf. Kawabata and Takafuji, 2005).

In summary, the Ramadas garnet compositions and textures are well in agreement with existing literature data (e.g. Clemens and Wall, 1981, 1988; Dahlquist et al., 2007; Harangi et al., 2001; Kawabata and Takafuji, 2005; Macleod, 1992) that demonstrate how Ca-poor (CaO < 4 wt%) and Mn-rich (MnO > 4 wt%) almandine garnet can crystallize from hydrous Mn-rich peraluminous silicic melts at shallow depths (1–1.5 kbar) for temperature higher or equal to 700 °C.

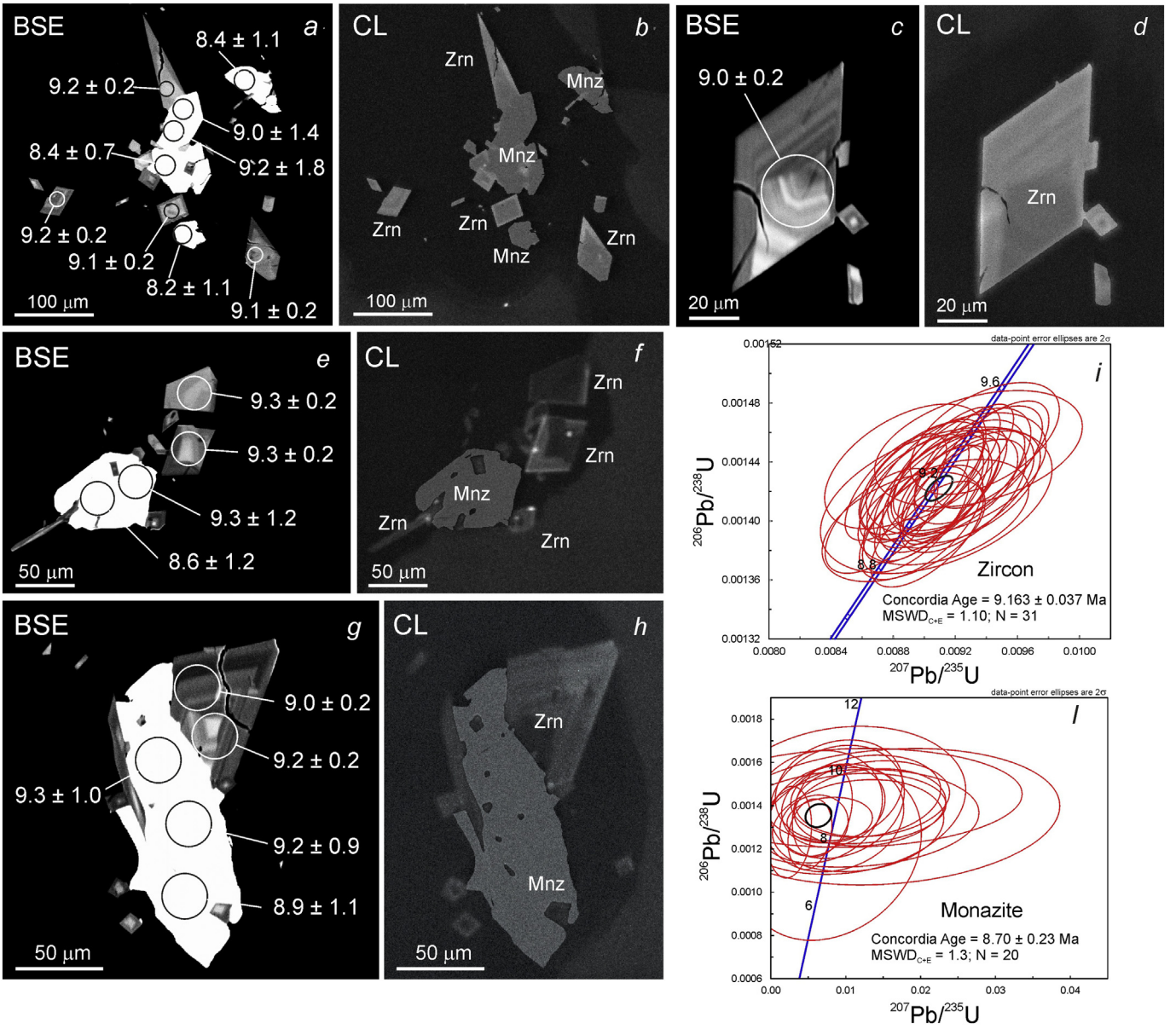

Fig. 5. U-(Th)-Pb zircon and monazite systematics for studied Ramadas tube-pumice samples. (a-h) Representative BSE and cathodoluminescence (CL) images of zircon (Zrn) and monazite (Mnz) grains from the studied samples, shown together with location of the LA-ICP-MS laser spots (white circles) and relative $^{206}Pb/^{238}U$ ages in Ma (errors quoted at 2σ level). (i) Conventional Concordia diagram showing the cumulative zircon data. (l) Conventional Concordia diagram showing cumulative monazite data. $MSWD_{C+E}$ is the mean square weighted deviation for concordance and equivalence.

8.2. Phase-meltREE partitioning

In a garnet-zircon- melt system, the garnet and zircon REE behaviors and their phase/melt partitioning are key-factors in understanding magmatic equilibria and to link rock textures to geochronology (e.g., Rubatto, 2002; Rubatto and Hermann, 2007; Taylor et al., 2015; Taylor et al., 2017). To verify the magmatic equilibria between garnet, zircon and glass in the Ramadas rhyolites, mineral/melt and mineral/mineral REE distribution coefficients are calculated from the analyzed material and then compared to the existing literature (Buick et al., 2006; Harley et al., 2001; Hermann and Rubatto, 2003; Hokada and Harley, 2004; Kelly and Harley, 2005; Rubatto, 2002; Rubatto and Hermann, 2007; Taylor et al., 2015; Whitehouse and Platt, 2003). The basic assumptions done in this study are: (i) pumice glass is the residual melt after garnet (+ zircon + monazite) crystallization, and (ii) all the Zr was initially dissolved in the original melt since the absence of inherited zircon grains and/or cores. Results are reported in Supplementary Table S4.

The REE distribution coefficients (D_{REEs}) calculated for zircon/melt (D: C^{Zrn}/C^{L}, where C^{Zrn} is the element concentration in zircon and C^{L} is the element concentration in "glass" sample) and garnet/melt (D: C^{Grt}/C^{L}, where C^{Grt} is the element concentration in garnet and C^{L} is the element concentration in "glass" sample) indicate the LREE are strongly partitioned into melt, whereas medium to HREE are primarily partitioned in zircon and garnet (Fig. 7).

Given the absence of extensive studies on absolute and pressure-temperature dependence of zircon-melt D_{REEs} for what concerns the LREE behavior in zircon (Geisler et al., 2007; Hanchar and Van Westrenen, 2007), we focus our discussion on medium to heavy REE (from Sm to Lu) budget. The zircon/garnet D_{REE} distribution coefficients (D: C^{Zrn}/C^{Grt}) were calculated comparing all zircon analyses to all garnet compositions (see also Taylor et al., 2017). Calculated coefficients are reported in Supplementary Table S4 and presented in Fig. 8. The zircon/garnet D_{REE} show concave-up profiles, characterized by Eu and HREE

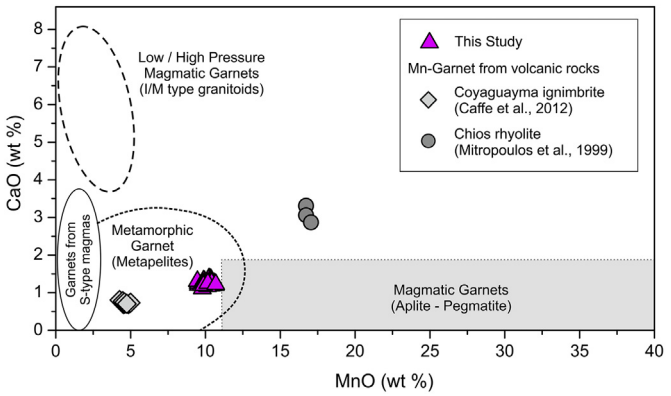

Fig. 6. CaO vs. MnO diagram (modified after Harangi et al., 2001; Samadi et al., 2014) for garnets from Ramadas tube-pumices. Mn-garnets from Coyaguayma ignimbrite (northern Puna, Argentina, Miocene in age; Caffe et al., 2012) and Chios rhyolite (Cyclades, Greece, Neogene in age; Mitropoulos et al., 1999) are also reported for comparison.

favoring zircon over garnet, with Yb/Dy and Lu/Gd up to 3.6 and 6.8, respectively (Fig. 8).

Considering the Ti-in-Zircon thermometry results (mean value of 785 ± 70 °C), the D_{HREEs} zircon/garnet profiles are substantially in agreement with those obtained in high-temperature melting experiments of Rubatto and Hermann (2007) and with the empirical studies of Rubatto (2002), Herman and Rubatto (2003) and Buick et al. (2006) (Fig. 8). This evidence confirms a common magmatic origin from the same original parental melt for both garnet and zircon, at equilibrium with the residual liquid here represented by the rhyolitic glass.

8.3. Timing, rates and longevity of the magmatic plumbing system

Investigating the origin of this high-peraluminous rhyolitic melt is beyond the scope of this work. However, a possible anatectic origin for the Ramadas garnet-bearing rhyolitic melt is suggested by: (i) the monogenetic character of the Ramadas Volcanic Centre (i.e. absence of a line of descent); (ii) its solitary setting in basement rocks; and (iii) the existing Sr-Nd isotope data (Viramonte et al., 1984, 2007).

Despite the uncertainty on the thermo-baric estimates, results of this study permit to define the timing and longevity of the Ramadas magmatic plumbing system, as shown in the temperature–time diagram of Fig. 9. The RVC history started with the assembly in the upper crust (< 6 km depth) of a peraluminous rhyolitic melt at a temperature of ca. 785 ± 70 °C (Ti-in-zircon thermometry), shortly before 9.16 ± 0.04 Ma as constrained by the U-Pb age of the zircons. Zircons acted as nucleation seeds for garnets growth at $T > 700$ °C (absence of Fe-Mn-Mg zoning in garnet). The garnet growth spans across a decrease in temperature of ca. 100 °C within the U-Pb closure temperature windows for zircon and monazite, as constrained by the monazite-solubility model thermometry (670 ± 25 °C), and by the monazite U-(Th)-Pb age of 8.70 ± 0.23 Ma. Furthermore, the agreement of temperatures (± 25 °C) obtained by the independently calibrated REE- and Zr-solubility models suggests that monazite and zircon were extracted from the felsic melt by the same magmatic event. In particular, the monazite U-(Th)-Pb age (8.70 ± 0.23 Ma) overlaps with the available K-Ar geochronological data from the CBT pumices (Petrinovic et al., 1999; Viramonte et al., 1994), suggesting it records the timing of the Ramadas eruption event (Fig. 9).

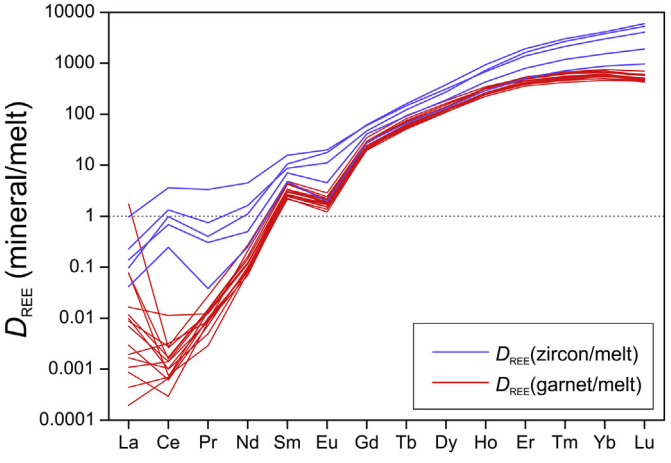

Fig. 7. D_{REE} (mineral/melt) data for the Ramadas tube-pumices.

The lack of Fe-Mn-Mg zoning in garnet suggests self-diffusion and re-equilibration of the garnet composition at high temperature (Dahlquist et al., 2007 and references therein). Diffusivities for Fe, Mg, Ca and Mn in garnet can differ by several orders of magnitude for a given temperature, with Ca being the slowest diffusing component (Carlson, 2006; Villaros et al., 2009b and references therein). Using the Carlson (2006) diffusivity data for Fe, Mg, Mn and Ca (at $T = 750$–800 °C and $P < 5$ kbar) and the equation $[t = x^2 \times t'/D]$ of Crank (1975), where t' is a dimensionless time parameter (0.4 for sphere) and D is the diffusion rate (m^2/s), the time t necessary for elements to diffuse in a spherical crystal of radius x can be obtained. Results show the time required to homogenize a garnet of radius ≈ 300 μm is in the range of 114–361 kyr (average: 237 ± 124 kyr) for Fe, Mg and Mn, whereas one order of magnitude higher (1.14–3.61 Myr) is necessary for Ca. The Fe-Mg-Mn diffusion-homogenization time window of 237 ± 124 kyr is in excellent overlap with the time-window of 460 ± 270 kyr as constrained by the U-(Th)-Pb dating of zircon and monazite inclusions in garnet, suggesting this time-window represents the minimum residence time of garnet in the melt.

The H_2O content of 3–5 wt%, calculated with the monazite-solubility model, indicates that Ramadas rhyolite melt was at pressures of 1–1.5 kb (water-solubility in silicate melts, after Wallace and Anderson, 2000; Mn-rich almandine chemistry, Clemens and Wall, 1981, 1988; Kawabata and Takafuji, 2005), corresponding to a depth < 6 km. At such volatile concentrations, together with very low crystal content (1 vol%), effective viscosity of rhyolitic melt can be as low as 10^6 Pa s (Giordano et al., 2008). The summarized conditions of temperature (ca. 660 ± 25 °C), volatile content (ca. 3–5 wt%) and viscosity (ca. 10^6 Pa s) are, in our interpretations, the immediately pre-eruptive magma properties that explain the unique and extremely high ascent

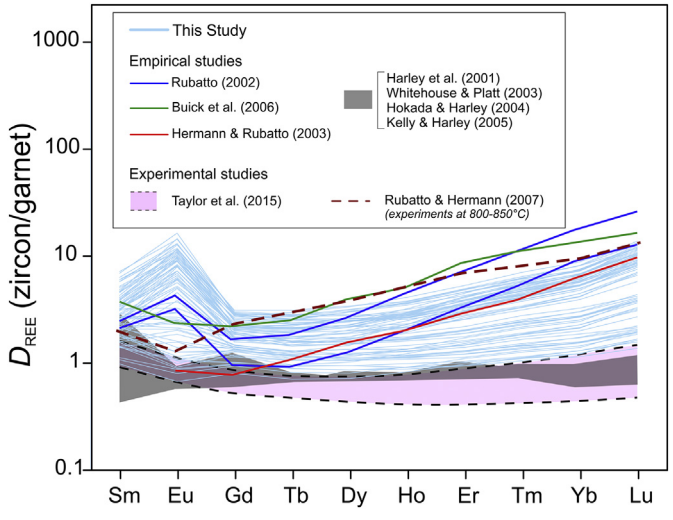

Fig. 8. D_{REE} (zircon/garnet) data for the Ramadas tube-pumices as compared with the D_{REE} (zircon/garnet) values from literature (Buick et al., 2006; Harley et al., 2001; Hermann and Rubatto, 2003; Hokada and Harley, 2004; Kelly and Harley, 2005; Rubatto, 2002; Rubatto and Hermann, 2007; Taylor et al., 2015; Whitehouse and Platt, 2003).

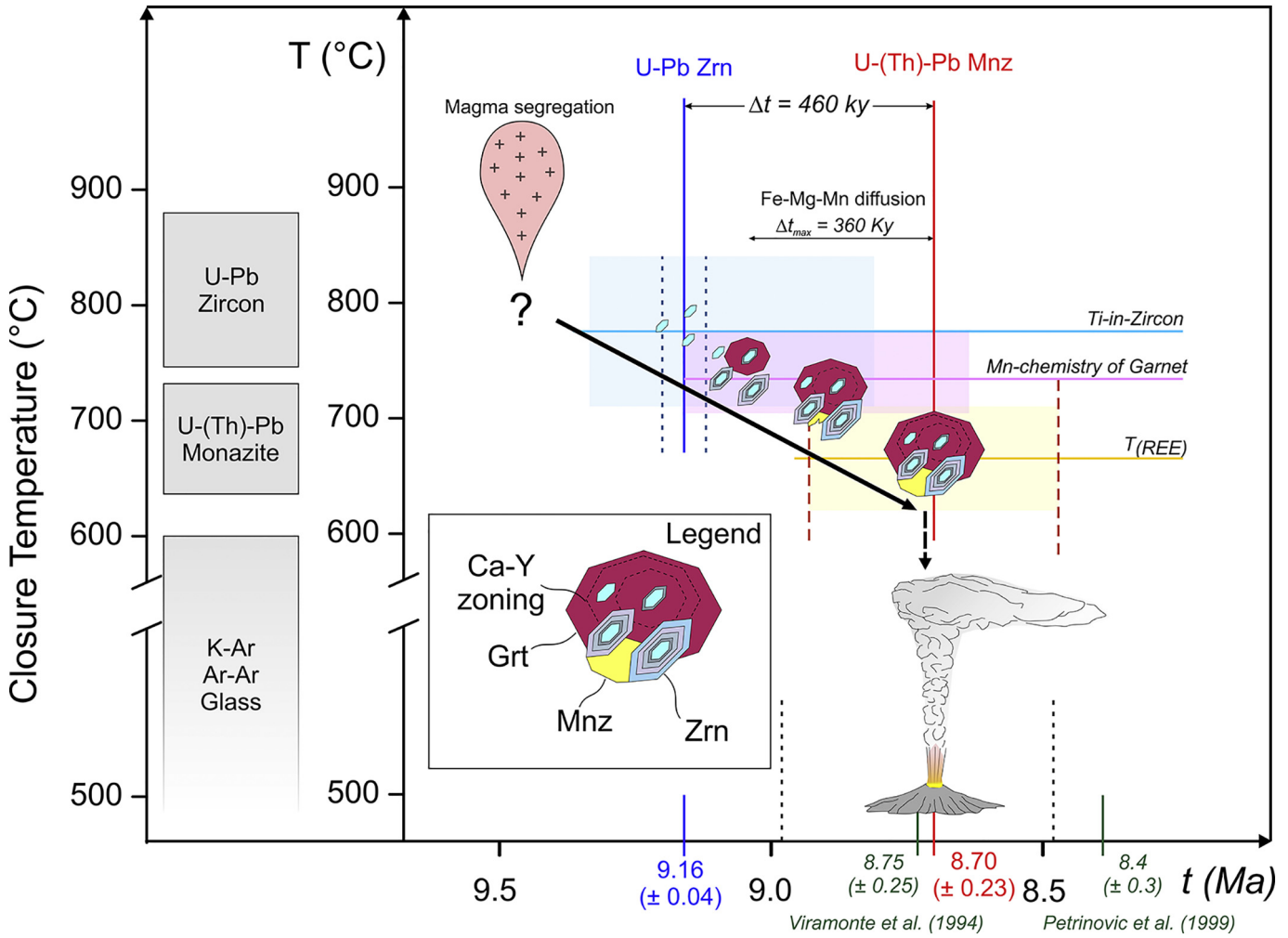

Fig. 9. Conceptual Temperature-time (*T-t*) model for the evolution of the magmatic plumbing system of the Ramadas Volcanic Centre, from liquidus, melt crystallization to the Plinian eruption (Corte Blanco Tuff). Existing K-Ar ages (8.75 ± 0.25 Ma after Viramonte et al. (1994) and 8.4 ± 0.3 Ma after Petrinovic et al. (1999), respectively) are also reported in green. Closure temperatures for the different isotope systems are also indicated (after Carlson, 2011). (For interpretation of the references to colour in this figure legend, the reader is referred to the web version of this article.)

rates inferred for the Ramadas CBT tube pumice (Dingwell et al., 2016; Marti et al., 1999).

While the presented thermo-baric reconstruction for the Ramadas melt relies on a large and consistent dataset, we note that the estimated monazite-solubility temperature of ca. 660 °C is close to the solidus. However, the very low degree of crystallization suggests instead that the temperature conditions at the time of eruption were quite far from the solidus. This evidence confirms the uniqueness of the Ramadas melts and should foster experimental studies to model the thermo-baric and physical-chemical environment of its formation and its crystallization history across the solidus.

9. Conclusion

The magmatic garnet-zircon-monazite-glass assemblage from the RVC constitutes a unique natural laboratory to unravel magmatic processes building up conditions for large volume Plinian eruptions to an unprecedented resolution.

The main outcomes of this study are: (i) the clear identification of the magmatic origin of the garnet phenocrysts; (ii) the reconstruction of the temperature window (785–670 °C) and pressure conditions (1–1.5 kbar) for the pre-eruptive storage and evolution of the Ramadas melt; and (iii) the assessment of the longevity of the magmatic plumbing system, from early melt crystallization started at 9.16 ± 0.04 Ma up to its eruption at 8.70 ± 0.23 Ma.

Finally, the geochemical characteristics of the garnet phenocrysts and their inclusion assemblage have the potential to decode the time-space scales and physical-chemical processes involved in the genesis of the magmatic plumbing system leading to major eruptive events.

Supplementary data to this article can be found online at https://doi.org/10.1016/j.lithos.2018.10.016.

Acknowledgments

The authors are grateful to two anonymous reviewers and the Editor (Dr. A. Kerr) for their helpful comments and suggestions that greatly helped to improve the manuscript. Authors also thank M. Soligo and G. Della Ventura for discussion and advice. Authors acknowledge the support of Consejo de Investigación de la UNSa, CONICET and FONCyT. The field and sampling work were partially financially supported by Grants PICT 2014-3436 FONCyT (ANPCyT) and CIUNSa 2314/0 and 2390/0.

References

Bea, F., Pereira, M.D., Stroh, A., 1994. Mineral/leucosome trace-element partitioning in a peraluminous migmatite (a laser ablation-ICP-MS study). Chem. Geol. 117 (1–4), 291–312.

Belousova, E., Griffin, W.L., O'Reilly, S.Y., Fisher, N.L., 2002. Igneous zircon: trace element composition as an indicator of source rock type. Contrib. Mineral. Petrol. 143 (5), 602–622.
Buick, I.S., Hermann, J., Williams, I.S., Gibson, R.L., Rubatto, D., 2006. A SHRIMP U–Pb and LA-ICP-MS trace element study of the petrogenesis of garnet–cordierite–orthoamphibole gneisses from the Central Zone of the Limpopo Belt, South Africa. Lithos 88 (1–4), 150–172.
Caffe, P.J., Trumbull, R.B., Siebel, W., 2012. Petrology of the Coyaguayma ignimbrite, northern Puna of Argentina: Origin and evolution of a peraluminous high-SiO 2 rhyolite magma. Lithos 134, 179–200.
Carlson, W.D., 2006. Rates of Fe, Mg, Mn, and Ca diffusion in garnet. Am. Mineral. 91 (1), 1–11.
Carlson, R.W., 2011. Absolute age determinations: radiometric. Encyclopedia of Solid Earth Geophysics. Springer, Netherlands, pp. 1–8.
Casas, A., Hernandez, E., Marti, J., Petrinovic, I., 1995. Gravity modelling of the Ramadas Caldera (Argentinean Puna, Central Andes). Expanded Abstracts. VOL. 4. Congresso Internacional Da Sociedade Brasileira de Geofisica, Rio de Janeiro (August 1995).
Cesare, B., Mariani, E.S., Venturelli, G., 1997. Crustal anatexis and melt extraction during deformation in the restitic xenoliths at El Joyazo (SE Spain). Min. Mag. 61 (1), 15–27.
Clemens, J.D., Wall, V.J., 1981. Origin and crystallization of some peraluminous (S-type) granitic magmas. Can. Mineral. 19, 111–131.
Clemens, J.D., Wall, V.J., 1984. Origin and evolution of a peraluminous silicic ignimbrite suite: the Violet Town Volcanics. Contrib. Mineral. Petrol. 88 (4), 354–371.
Clemens, J.D., Wall, V.J., 1988. Controls on the mineralogy of S-type volcanic and plutonic rocks. Lithos 21, 53–66.
Coira, B., Kay, S.M., Viramonte, J.G., Kay, R.G., Galli, C., 2018. Origin of late Miocene peraluminous Mn-rich garnet-bearing rhyolitic ashes in the Andean foreland (Northern Argentina). J. Volcanol. Geotherm. Res. https://doi.org/10.1016/j.jvolgeores.2018.08.020.
Corfu, F., Hanchar, J.M., Hoskin, P.W., Kinny, P., 2003. Atlas of zircon textures. Rev. Mineral. Geochem. 53 (1), 469–500.
Crank, J., 1975. The Mathematics of Diffusion. Oxford University Press (Eds), Oxford (414pp).
Dahlquist, J.A., Galindo, C., Pankhurst, R.J., Rapela, C.W., Alasino, P.H., Saavedra, J., Fanning, C.M., 2007. Magmatic evolution of the Peñón Rosado granite: petrogenesis of garnet-bearing granitoids. Lithos 95 (3–4), 177–207.
Dingwell, D.B., Lavallée, Y., Hess, K.U., Flaws, A., Marti, J., Nichols, A.R.L., Gilg, H.A., Schillinger, B., 2016. Eruptive shearing of tube pumice: pure and simple. Solid Earth Discuss. 7 (4).
Enami, M., Cong, B., Yoshida, T., Kawabe, I., 1995. A mechanism for Na incorporation in garnet: an example from garnet in orthogneiss from the Su-Lu terrane, eastern China. Am. Mineral. 80 (5–6), 475–482.
Evans, B.W., Trommsdorff, V., 1978. Petrogenesis of garnet lherzolite, Cima di Gagnone, Lepontine Alps. Earth Planet. Sci. Lett. 40 (3), 333–348.
Ferry, J.M., Watson, E.B., 2007. New thermodynamic models and revised calibrations for the Ti-in-zircon and Zr-in-rutile thermometers. Contrib. Mineral. Petrol. 154 (4), 429–437.
Gadas, P., Novák, M., Talla, D., Galiová, M.V., 2013. Compositional evolution of grossular garnet from leucotonalitic pegmatite at Rudanad Moravou, Czech Republic; a complex EMPA, LA-ICP-MS, IR and CL study. Mineral. Petrol. 107 (2), 311–326.
Gauthier, P.J., Déruelle, B., Viramonte, J.G., Aparicio, A., 1994. Grenats des rhyolites de la caldera de La Pava—Ramadas (NW Argentine) et de leurs xenolites granitiques. CR Acad. Sci. 318, 1629–1635.
Geisler, T., Schaltegger, U., Tomaschek, F., 2007. Re-equilibration of zircon in aqueous fluids and melts. Elements 3 (1), 43–50.
Giordano, D., Russell, J.K., Dingwell, D.B., 2008. Viscosity of magmatic liquids: a model. Earth Planet. Sci. Lett. 271 (1–4), 123–134.
Giordano, G., Pinton, A., Cianfarra, P., Baez, W., Chiodi, A., Viramonte, J., Norini, G., Groppelli, G., 2013. Structural control on geothermal circulation in the Cerro Tuzgle–Tocomar geothermal volcanic area (Puna plateau, Argentina). J. Volcanol. Geotherm. Res. 249, 77–94.
Hanchar, J.M., Van Westrenen, W., 2007. Rare earth element behavior in zircon-melt systems. Elements 3 (1), 37–42.
Harangi, S.Z., Downes, H., Kósa, L., Szabó, C.S., Thirlwall, M.F., Mason, P.R.D., Mattey, D., 2001. Almandine garnet in calc-alkaline volcanic rocks of the Northern Pannonian Basin (Eastern–Central Europe): Geochemistry, petrogenesis and geodynamic implications. J. Petrol. 42 (10), 1813–1843.
Harley, S. L., Kinny, P., Snape, I., and Black, L. P. (2001). Zircon chemistry and the definition of events in Archaean granulite terrains. In: Fourth International Archaean Symposium, Extended Abstract Volume, AGSO Geoscience Australia Record,vol. 37, 511–513.
Harley, S.L., Kelly, N.M., Möller, A., 2007. Zircon behaviour and the thermal histories of mountain chains. Elements 3 (1), 25–30.
Harrison, T.N., 1988. Magmatic garnets in the Cairngorm granite, Scotland. Min. Mag. 52 (368), 659–667.
Hermann, J., Rubatto, D., 2003. Relating zircon and monazite domains to garnet growth zones: age and duration of granulite facies metamorphism in the Val Malenco lower crust. J. Metamorph. Geol. 21 (9), 833–852.
Hokada, T., Harley, S.L., 2004. Zircon growth in UHT leucosome: constraints from zircon-garnet rare earth elements (REE) relations in Napier complex, East Antarctica. J. Mineral. Petrol. Sci. 99 (4), 180–190.
Hönig, S., Čopjaková, R., Škoda, R., Novák, M., Dolejš, D., Leichmann, J., Galiová, M.V., 2014. Garnet as a major carrier of the Y and REE in the granitic rocks: an example from the layered anorogenic granite in the Brno Batholith, Czech Republic. Am. Mineral. 99 (10), 1922–1941.
Hoskin, P.W., Schaltegger, U., 2003. The composition of zircon and igneous and metamorphic petrogenesis. Rev. Mineral. Geochem. 53 (1), 27–62.
Kawabata, H., Takafuji, N., 2005. Origin of garnet crystals in calc-alkaline volcanic rocks from the Setouchi volcanic belt, Japan. Min. Mag. 69 (6), 951–971.
Kelly, N.M., Harley, S.L., 2005. An integrated microtextural and chemical approach to zircon geochronology: refining the Archaean history of the Napier complex, East Antarctica. Contrib. Mineral. Petrol. 149 (1), 57–84.
Lackey, J.S., Romero, G.A., Bouvier, A.S., Valley, J.W., 2012. Dynamic growth of garnet in granitic magmas. Geology 40 (2), 171–174.
London, D., 2008. Pegmatites. Can. Mineral. 10, 347.
Ludwig, K., 2010. Isoplot/Ex Version 4.1, a Geochronological Toolkit for Microsoft Excel. Berkeley Geochronology Center Special Publication, Berkeley, CA, USA (4).
Ma, L., Wang, Q., Kerr, A.C., Yang, J.H., Xia, X.P., Ou, Q., Yang, Z.-Y., Sun, P., 2017. Paleocene (c. 62 Ma) Leucogranites in Southern Lhasa, Tibet: Products of Syn-collisional Crustal Anatexis during Slab Roll-back? J. Petrol. 58 (11), 2089–2114.
Macleod, G., 1992. Zoned manganiferous garnets of magmatic origin from the Southern Uplands of Scotland. Min. Mag. 56 (382), 115–116.
Manning, D.A.C., 1983. Chemical variation in garnets from aplites and pegmatites, peninsular Thailand. Min. Mag. 47, 353–358.
Marti, J., Soriano, C., Dingwell, D.B., 1999. Tube pumices as strain markers of the ductile–brittle transition during magma fragmentation. Nature 402 (6762), 650.
Miller, C.F., Stoddard, E.F., 1981. The role of manganese in the paragenesis of magmatic garnet: an example from the Old Woman-Piute Range, California. J. Geol. 89 (2), 233–246.
Miller, C.F., McDowell, S.M., Mapes, R.W., 2003. Hot and cold granites? Implications of zircon saturation temperatures and preservation of inheritance. Geology 31 (6), 529–532.
Mitropoulos, P., Katerinopoulos, A., Kokkinakis, A., 1999. Occurrence of primary almandine-spessartine-rich garnet and zinnwaldite phenocrysts in a Neogene rhyolite on the island of Chios, Aegean Sea, Greece. Min. Mag. 63 (4), 503–510.
Montel, J.M., 1993. A model for monazite/melt equilibrium and application to the generation of granitic magmas. Chem. Geol. 110 (1–3), 127–146.
Müller, A., Kearsley, A., Spratt, J., Seltmann, R., 2012. Petrogenetic implications of magmatic garnet in granitic pegmatites from southern Norway. Can. Mineral. 50 (4), 1095–1115.
Oliver, R.L., 1956. The origin of garnets in the Borrowdale Volcanic Series and associated rocks, English Lake District. Geol. Mag. 93 (2), 121–139.
Patranabis-Deb, S., Schieber, J., Basu, A., 2009. Almandine garnet phenocrysts in a~ 1 Ga rhyolitic tuff from Central India. Geol. Mag. 146 (1), 133–143.
Petrinovic, I.A., Mitjavila, J., Viramonte, J.G., Martí, J., Becchio, R., Arnosio, M., Colombo, F., 1999. Descripcióngeoquímica y geocronológica de secuenciasvolcánicasneógenas de Trasarco, en elextremooriental de la CadenaVolcánicaTransversal del Quevar (Noroeste de Argentina). Acta Geológicahispánica 34 (2), 255–272.
Rapp, R.P., Watson, E.B., 1986. Monazite solubility and dissolution kinetics: implication for the Th and light rare-earth chemistry of felsic magmas. Contrib. Mineral. Petrol. 94, 304–316.
Rossetti, F., Tecce, F., Billi, A., Brilli, M., 2007. Patterns of fluid flow in the contact aureole of the late Miocene Monte Capanne pluton (Elba Island, Italy): the role of structures and rheology. Contrib. Mineral. Petrol. 153 (6), 743–760.
Rubatto, D., 2002. Zircon trace element geochemistry: partitioning with garnet and the link between U–Pb ages and metamorphism. Chem. Geol. 184 (1–2), 123–138.
Rubatto, D., Hermann, J., 2003. Zircon formation during fluid circulation in eclogites (Monviso, Western Alps): implications for Zr and Hf budget in subduction zones. Geochim. Cosmochim. Acta 67 (12), 2173–2187.
Rubatto, D., Hermann, J., 2007. Experimental zircon/melt and zircon/garnet trace element partitioning and implications for the geochronology of crustal rocks. Chem. Geol. 241 (1–2), 38–61.
Samadi, R., Miller, N.R., Mirnejad, H., Harris, C., Kawabata, H., Shirdashtzadeh, N., 2014. Origin of garnet in aplite and pegmatite from KhajehMorad in northeastern Iran: a major, trace element, and oxygen isotope approach. Lithos 208, 378–392.
Smeds, S.A., 1994. Zoning and fractionation trends of a peraluminous NYF granitic pegmatite field at Falun, south-Central Sweden. GFF 116 (3), 175–184.
Spear, F.S., 1993. Metamorphic Phase Equilibria and Pressure-Temperature-Time Paths. Monograph, Mineralogical Society of America, Washington D.C, p. 799.
Sun, S.S., McDonough, W.S., 1989. Chemical and Isotopic Systematics of Oceanic Basalts: Implications for Mantle Composition and Processes. vol. 42. Geological Society, London, Special Publications, pp. 313–345 1.
Tait, M.A., Cas, R.A.F., Viramonte, J.G., 2009. The origin of an unusual tuff ring of perlitic rhyolite pyroclasts: the last explosive phase of the Ramadas Volcanic Centre, Andean Puna, Salta, NW Argentina. J. Volcanol. Geotherm. Res. 183 (1–2), 1–16.
Taylor, J., Stevens, G., 2010. Selective entrainment of peritectic garnet into S-type granitic magmas: evidence from Archaean mid-crustal anatectites. Lithos 120 (3–4), 277–292.
Taylor, R.J.M., Harley, S.L., Hinton, R.W., Elphick, S., Clark, C., Kelly, N.M., 2015. Experimental determination of REE partition coefficients between zircon, garnet and melt: a key to understanding high-T crustal processes. J. Metamorph. Geol. 33 (3), 231–248.
Taylor, R.J.M., Clark, C., Harley, S.L., Kylander-Clark, A.R.C., Hacker, B.R., Kinny, P.D., 2017. Interpreting granulite facies events through rare earth element partitioning arrays. J. Metamorph. Geol. 35, 759–775.
Villaros, A., Stevens, G., Moyen, J.F., Buick, I.S., 2009a. The trace element compositions of S-type granites: evidence for disequilibrium melting and accessory phase entrainment in the source. Contrib. Mineral. Petrol. 158 (4), 543–561.
Villaros, A., Stevens, G., Buick, I.S., 2009b. Tracking S-type granite from source to emplacement: clues from garnet in the Cape Granite Suite. Lithos 112 (3–4), 217–235.
Viramonte, J.G., Omarini, R.H., Araña Saavedra, V., Aparicio, A., García Cacho, L., Parica, P., 1984. Edad génesis y mecanismos de erupción de las riolítas granatíferas de San Antonio de Los Cobres, provincia de Salta. IX Congreso Geológico Argentino. Vol. 3, pp. 216–233.
Viramonte, J., Reynolds, J.H., Del Papa, C., Disalvo, A., 1994. The Corte Blanco garnetiferous tuff: a distinctive late Miocene marker bed in northwestern Argentina applied to

magnetic polarity stratigraphy in the Rio Yacones, Salta Province. Earth Planet. Sci. Lett. 121 (3–4), 519–531.
Viramonte, J.M., Viramonte, J.G., Becchio, R., Pimentel, M., Arnosio, M., 2007. Ramadas Volcanic Centre (NW Argentina): Linking Between the Miocene Volcanism and the Lower Paleozoic Basement. 20th Colloquium on Latin American Earth Sciences (LAK) (Kiel-Germany). Abstract, pp. 62–63.
Wallace, P., and Anderson, A. T. Jr (2000) Volatiles in Magmas, Encyclopedia of Volcanoes, 149–170.
Wang, R., Hu, H., Zhang, A., Xu, S., Wang, D., 2003. Yttrium zoning in garnet from the Xihuashan granitic complex and its petrological implications. Chin. Sci. Bull. 48 (15), 1611–1615.
Watson, E.B., Harrison, T.M., 1983. Zircon saturation revisited: temperature and composition effects in a variety of crustal magma types. Earth Planet. Sci. Lett. 64 (2), 295–304.
Watson, E.B., Wark, D.A., Thomas, J.B., 2006. Crystallization thermometers for zircon and rutile. Contrib. Mineral. Petrol. 151 (4), 413.
White, R.W., Powell, R., Johnson, T.E., 2014. The effect of Mn on mineral stability in metapelites revisited: new a–x relations for manganese-bearing minerals. J. Metamorph. Geol. 32 (8), 809–828.
Whitehouse, M.J., Platt, J.P., 2003. Dating high-grade metamorphism—constraints from rare-earth elements in zircon and garnet. Contrib. Mineral. Petrol. 145 (1), 61–74.
Whitney, D.L., Evans, B.W., 2010. Abbreviations for names of rock-forming minerals. Am. Min. 95 (1), 185–187.
Wood, C.P., 1974. Petrogenesis of garnet-bearing rhyolites from Canterbury, New Zealand. N. Z. J. Geol. Geophys. 17 (4), 759–787.
Wyborn, D., Chappell, B.W., Johnston, R.M., 1981. Three S-type volcanic suites from the Lachlan Fold Belt, Southeast Australia. J. Geophys. Res. 86 (B11), 10335–10348.
Yardley, B.W.D., 1977. An empirical study of diffusion in garnet. Am. Mineral. 62, 793–800.
Zhang, R.Y., Liou, J.G., Cong, B., 1994. Petrogenesis of garnet-bearing ultramafic rocks and associated eclogites in the Su-Lu ultrahigh-P metamorphic terrane, eastern China. J. Metamorph. Geol. 12 (2), 169–186.
Zhou, J., Feng, C., Li, D., 2017. Geochemistry of the garnets in the Baiganhu W–Sn orefield, NW China. Ore Geol. Rev. 82, 70–92.